Bone 209 (2026) 117905

Contents lists available at ScienceDirect

Bone

journal homepage: www.elsevier.com/locate/bone

Full Length Article

Factors of mineralization dynamics — A mathematical model for microstructural bone remodeling

Corinna Modiz [a,b,*], Natalia M. Castoldi [a,c], Jose L. Calvo-Gallego [d,e], Stefan Scheiner [f], Vittorio Sansalone [b], Saulo Martelli [a], Javier Martínez-Reina [d,e], Peter Pivonka [a]

[a] School of Mechanical, Medical and Process Engineering, Queensland University of Technology, Brisbane, 4000, Queensland, Australia
[b] Univ Paris Est Creteil, Univ Gustave Eiffel, CNRS, UMR 8208, MSME, F-94010, Créteil, France
[c] Faculty of Mechanical Engineering, Technische Hochschule Georg Simon Ohm, 90489, Nürnberg, Germany
[d] Departmento de Ingeniería Mecánica y Fabricación, Universidad de Sevilla, 41092, Sevilla, Spain
[e] Instituto de Biomedicina de Sevilla (IBIS), C/ Antonio Maura Montaner, 41013, Sevilla, Spain
[f] Institute for Mechanics of Materials and Structures, TU Wien, 1040, Vienna, Austria

ARTICLE INFO

Keywords:
Bone mineralization dynamics
Bone porosity
Mathematical modeling
Trabecular-cortical variations
Specific surface
Turnover rate
Mineral apposition rate
Trabecular microarchitecture

ABSTRACT

Bone mineralization critically influences bone strength and fracture risk, yet the dependency on bone porosity across the range from cortical to trabecular bone remains incompletely understood. We present a novel mathematical framework that explicitly models bone mineralization dynamics as a function of bone turnover, which can be linked to porosity. Unlike existing fixed-porosity models, our approach incorporates porosity-dependent cellular activity based on remodeling surface availability, enabling analysis across the entire porosity range. We tested three biologically motivated hypotheses to explain mineral content variations with porosity, involving variations in turnover rate, targeted resorption and mineral apposition rate. Through systematic hypothesis testing validated against experimental data, we successfully reproduced the characteristic relationship between material and apparent density observed across varying bone porosities. Results indicate that porosity-dependent turnover and mineral apposition rate primarily drive mineralization. Global sensitivity analysis confirmed the mineral apposition rate as the most influential parameter. Additionally, our analysis supports that dispersion in mid-porosity experimental data can be explained by trabecular microarchitectural variations, specifically the proportion of rod-like versus plate-like structures affecting specific surface area. This framework provides a mechanistic explanation for bone mineralization variations across the porosity range.

1. Introduction

Compromised bone quality is a primary determinant of fracture risk, particularly in osteoporosis where anti-resorptive therapies increase mineral density [1–4] but may suppress remodeling, leading to older, more brittle tissue over time. Bone quality is a multiscale attribute involving microarchitecture, remodeling dynamics, and mineral content [1]. Bone mineralization dynamics are particularly important for the elastic modulus and fracture resistance of bone tissue [5–7], but remain incompletely understood.

Bone remodeling is the fundamental process involving bone resorption by osteoclasts and formation by osteoblasts to maintain bone quality and calcium homeostasis. Under normal physiological conditions, bone homeostasis is maintained through balanced remodeling in which the amount of bone resorbed equals the amount of bone formed [8]. The last phase of bone remodeling is mineralization, where ions precipitate to form hydroxyapatite ($Ca_{10}(PO_4)_6(OH)_2$) in the newly formed osteoid. [9]. Rapid primary mineralization rapidly occurs after osteoid formation, reaching approximately 50% of the final mineral content, followed by slower secondary mineralization [2].

Variations in biomechanical properties, microarchitecture, physicochemical environments, and loading requirements between trabecular and cortical bone suggest different mineralization processes [10–12]. Cortical bone consists of dense osteons with direct vascular supply, while trabecular bone forms a less dense network that relies on diffusion for mineral exchange [13], affecting the availability of (Ca^{2+}) and (P_i) for hydroxyapatite precipitation [12]. Furthermore, variations in specific surface area – the bone surface available for cellular remodeling – dictate turnover rates [14,15]. The lower specific surface of cortical

* Corresponding author at: School of Mechanical, Medical and Process Engineering, Queensland University of Technology, Brisbane, 4000, Queensland, Australia.
E-mail address: corinna.modiz@hdr.qut.edu.au (C. Modiz).

https://doi.org/10.1016/j.bone.2026.117905
Received 5 August 2025; Received in revised form 26 March 2026; Accepted 22 April 2026
Available online 24 April 2026
8756-3282/© 2026 The Authors. Published by Elsevier Inc. This is an open access article under the CC BY license (http://creativecommons.org/licenses/by/4.0/).

Acronyms

BMDD	bone mineral density distribution
BCPM	bone cell population model
RVE	representative volume element
VOI	volume of interest
TGF-β	transforming growth factor β
RANK	receptor activator of nuclear factor $\kappa\beta$
RANKL	receptor activator of nuclear factor $\kappa\beta$ ligand
OPG	osteoprotegerin
PTH	parathyroid hormone
MCSF	macrophage colony stimulating factor
BMU	basic multicellular unit
LCN	lacunar-canalicular network
DMB	degree of mineralization of bone
BSU	bone structural unit
microCT	micro-computed tomography
FEA	finite element analysis

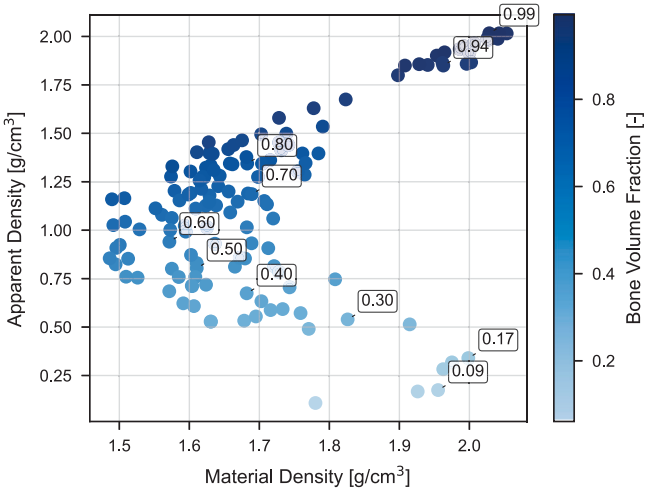


Fig. 1. Apparent density (Dn.app) vs. material density (Dn.mat) across the porosity range: The figure was generated using data tabulated by Berli et al. [24], originally reported by Zioupos et al. [23]. Markers are shaded and labeled by bone volume fraction ($f_{\mathrm{Tt.B}}$).

bone results in extended tissue aging, progressive mineral accumulation and higher degrees of mineralization [11]. These differences can also be observed in Bone Mineral Density Distribution (BMDD) analyses [16], which show a peak shift from trabecular to cortical bone, attributed to bone turnover rate and mineralization kinetics [11,16].

Boivin and Meunier's model proposed that bone turnover alone regulates bone matrix mineralization [17], with high turnover bone (trabecular) having lower mineralization than low turnover bone (cortical). Recent experimental findings challenge this model, highlighting the complexity of bone mineralization. Studying mineral accumulation in bone requires advanced imaging techniques to track changes over time [18]. Previous studies have shown differences in mineralization between trabecular and cortical bone [16,19–22], but most focus on fixed porosity values, limiting the analysis of mineralization dynamics across the porosity range. Zioupos et al. [23] addressed this gap by experimentally measuring mineral content across volumes of interest (VOIs) with varying porosity from one elephant femur. The specimen allows for high-resolution analysis of bone composition across a human-like structural organization [23]. They present a distinctive relationship between apparent density (bone mass per tissue volume) and material density (bone mass per bone matrix volume) in both trabecular and cortical VOIs across a porosity spectrum (Fig. 1). The boomerang-shaped curve suggests complex mineralization dynamics with systematic variations as porosity changes.

Mathematical modeling offers a complementary approach to studying mineralization dynamics and allows for exploring mechanisms that are difficult to access experimentally. Existing bone cell population models (BCPMs) have evolved from basic temporal dynamics [25–29] to include spatial dependencies [15] and mineralization [30]. Other modeling approaches analyzed BMDD variations and density relationships [24], but remain limited to fixed porosity values.

We extend these models by incorporating porosity-dependent cellular activity based on specific surface area [14,15] to analyze mineralization parameters across the full range of porosity. This enables a unified analysis of mineralization dynamics across the full porosity spectrum, rather than focusing solely on differences between trabecular and cortical bone. Building on previous work [16,17,24], we test three biologically motivated hypotheses:

Hypothesis 1 The differences in turnover rate – governed by porosity-dependent variations in available bone surface for remodeling – solely explain the observed mineral content variations with porosity.

Hypothesis 2 Combined effects of porosity-dependent turnover rate and targeted resorption in different bone compartments determine the mineral content variations with porosity. Targeted resorption refers to the preferential resorption of more highly mineralized (older) bone tissue by osteoclasts, while recently formed, less mineralized bone may be temporarily protected from resorption.

Hypothesis 3 Combined effects of porosity-dependent turnover rate and differences in mineralization kinetics, specifically the mineral apposition rate, determine mineral content variations.

To test these hypotheses, we use a computational model of bone remodeling in steady-state conditions (remodeling equilibrium). We address the following objectives:

- Develop a bone remodeling model linking mineralization and turnover rates to porosity, from trabecular to cortical bone.
- Implement a mineralization algorithm with varying kinetics and age-based targeted resorption.
- Validate the model against experimental data [23] to reproduce the characteristic density relationship and explain mid-range data dispersion.
- Identify key parameters for mineralization dynamics via global sensitivity analysis.

By linking porosity to mineralization dynamics, this study overcomes imaging limitations and provides the basis of multiscale bone quality assessment and the analysis of bone pathologies.

2. Methods

2.1. Mathematical model of mineralization in homeostasis

We integrate a porosity-dependent BCPM [15], which links cell concentration to bone turnover through the available specific surface area, with a mineral-tracking algorithm [30,31]. The latter tracks the mineral content of individual bone patches within a representative volume element (RVE) as they age. Typical RVE sizes are approximately $10 \times 2 \times 2$ mm for cortical bone [15] and $5 \times 5 \times 5$ mm for trabecular bone [32,33] — dimensions large enough to capture microstructural features such as Haversian canals and trabecular rods, yet small enough

to avoid macroscopic effects such as overall bone shape [34]. The model predicts density relationships across the porosity range to investigate the mechanisms underlying the characteristic boomerang-shaped curve.

2.1.1. Bone cell concentrations depending on porosity

To analyze mineral distributions across the porosity range, we adapt the BCPM by Lerebours et al. [15] to describe cell concentrations as a function of bone volume fraction ($f_{\mathrm{Tt.B}}$). The latter is defined at the RVE scale as bone volume per total volume ($f_{\mathrm{Tt.B}} = V_{\mathrm{Tt.B}}/V_{\mathrm{Tt.RVE}}$). It relates to the fraction of tissue scale porosity — defined as volume of pore space per volume of the RVE ($f_{\mathrm{Tt.Po}} = V_{\mathrm{Tt.Po}}/V_{\mathrm{Tt.RVE}} = 1 - f_{\mathrm{Tt.B}}$). Porosity includes the Haversian system in cortical bone and marrow spaces in trabecular bone.

While the original model simulated spatial adaptation to loading, we focus on a single RVE in steady state (bone remodeling in equilibrium without long-term changes in porosity). This simplification allows us to isolate how porosity levels and specific surface area influence cell population dynamics and mineralization under homeostatic conditions, regardless of spatial variations due to position-dependent mechanical loading.

The concentrations of active osteoclasts ($C_{\mathrm{Oc_a}}$) and osteoblasts ($C_{\mathrm{Ob_a}}$) are modeled through the differentiation of uncommitted ($\mathrm{Oc_u}, \mathrm{Ob_u}$) and pre-progenitor ($\mathrm{Oc_p}, \mathrm{Ob_p}$) populations. These dynamics are governed by intra-/inter-cellular communication pathways – including receptor activator of nuclear factor $\kappa\beta$ (RANK), the respective ligand (RANKL), transforming growth factor β (TGF-β), parathyroid hormone (PTH), and mechanical signals (S_{mech}) – which regulate differentiation ($\mathscr{D}$), apoptosis ($\mathscr{A}$), and proliferation rates ($\mathscr{P}$). The BCPM describes the temporal evolution of these populations as

$$
\begin{aligned}
\frac{\mathrm{d}}{\mathrm{d}t} C_{\mathrm{Oc_p}}(f_{\mathrm{Tt.B}}, t) &= \mathscr{D}_{C_{\mathrm{Oc_u}}}(C_{\mathrm{MCSF}}, C_{\mathrm{RANKL}}) \cdot C_{\mathrm{Oc_u}}(f_{\mathrm{Tt.B}}) \\
&\quad - \mathscr{D}_{C_{\mathrm{Oc_p}}}(C_{\mathrm{RANKL}}) \cdot C_{\mathrm{Oc_p}}, \\
\frac{\mathrm{d}}{\mathrm{d}t} C_{\mathrm{Oc_a}}(f_{\mathrm{Tt.B}}, t) &= \mathscr{D}_{C_{\mathrm{Oc_p}}}(C_{\mathrm{RANKL}}) \cdot C_{\mathrm{Oc_p}} - \mathscr{A}_{C_{\mathrm{Oc_a}}}(C_{\mathrm{TGF}\text{-}\beta}) \cdot C_{\mathrm{Oc_a}}, \\
\frac{\mathrm{d}}{\mathrm{d}t} C_{\mathrm{Ob_p}}(f_{\mathrm{Tt.B}}, t) &= \mathscr{D}_{C_{\mathrm{Ob_u}}}(C_{\mathrm{TGF}\text{-}\beta}) \cdot C_{\mathrm{Ob_u}}(f_{\mathrm{Tt.B}}) + \mathscr{P}_{C_{\mathrm{Ob_p}}}(S_{\mathrm{mech}}) \cdot C_{\mathrm{Ob_p}} \\
&\quad - \mathscr{D}_{C_{\mathrm{Ob_p}}}(C_{\mathrm{TGF}\text{-}\beta}) \cdot C_{\mathrm{Ob_p}}, \\
\frac{\mathrm{d}}{\mathrm{d}t} C_{\mathrm{Ob_a}}(f_{\mathrm{Tt.B}}, t) &= \mathscr{D}_{C_{\mathrm{Ob_p}}}(C_{\mathrm{TGF}\text{-}\beta}) \cdot C_{\mathrm{Ob_p}} - \mathscr{A}_{C_{\mathrm{Ob_a}}} \cdot C_{\mathrm{Ob_a}}.
\end{aligned} \tag{1}
$$

Concentrations C_X with $X \in \{$macrophage colony stimulating factor (MCSF), TGF-β, RANKL$\}$ and regulatory parameters follow standardized bone histomorphometry nomenclature [35]. Detailed mathematical formulations and parameter values are provided in the Supplementary Material.

For normal physiological conditions, we solve for steady-state concentrations by setting all temporal derivatives in Eq. (1) to zero. Lerebours' model relates cell concentrations and bone volume fraction through the turnover rate (TR, change of bone volume fraction per unit time). In homeostasis, the turnover rate reflects the balance between bone formation and resorption:

$$
\begin{aligned}
\mathrm{TR}(f_{\mathrm{Tt.B}}) &= \mathrm{BFR} \cdot C_{\mathrm{Ob_a}}(C_{\mathrm{Oc_u}}(f_{\mathrm{Tt.B}}), C_{\mathrm{Ob_u}}(f_{\mathrm{Tt.B}})) \\
&= \mathrm{BRs.R} \cdot C_{\mathrm{Oc_a}}(C_{\mathrm{Oc_u}}(f_{\mathrm{Tt.B}}), C_{\mathrm{Ob_u}}(f_{\mathrm{Tt.B}})),
\end{aligned} \tag{2}
$$

where BFR and BRs.R are the formation and resorption rates (bone volume fraction formed or resorbed per unit cell concentration and time). The relationship between active cells and bone volume fraction is mediated through uncommitted cell concentrations [15,36], reflecting the biological communication between cell lineages. Active osteoclasts release signaling factors (e.g., TGF-β) during resorption that influence osteoblast differentiation from the uncommitted pool, creating interdependence between both lineages' uncommitted populations. Using the explicit turnover rate derived in Section 2.1.2, we determine $C_{\mathrm{Ob_a}}(f_{\mathrm{Tt.B}})$ and $C_{\mathrm{Oc_a}}(f_{\mathrm{Tt.B}})$ before solving for the steady-state of (Eq. (1)) to calculate the remaining cell concentrations ($C_{\mathrm{Oc_u}}$, $C_{\mathrm{Oc_p}}$, $C_{\mathrm{Ob_u}}$, and $C_{\mathrm{Ob_p}}$).

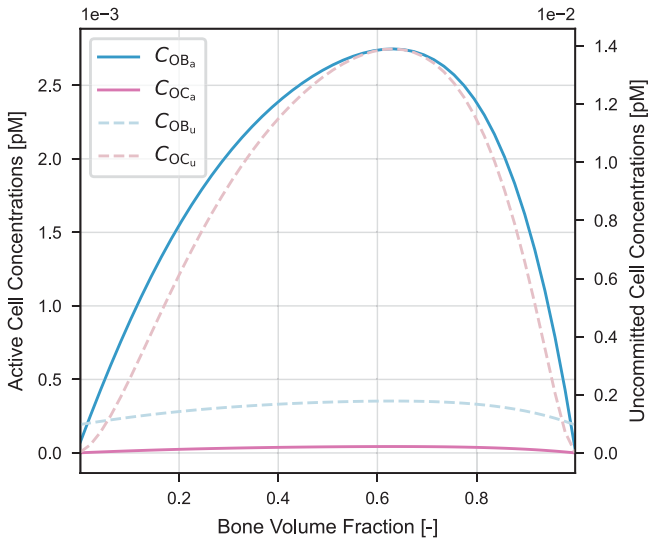


Fig. 2. Bone cell concentrations in steady-state: Concentration of active ($C_{\mathrm{Ob_a}}, C_{\mathrm{Oc_a}}$) and uncommitted ($C_{\mathrm{Ob_u}}, C_{\mathrm{Oc_u}}$) osteoblasts and osteoclasts depending on the bone volume fraction ($f_{\mathrm{Tt.B}}$), calculated from Eq. (2) and the equilibrium solution of Eq. (1).

The concentrations peak at $f_{\mathrm{Tt.B}} \approx 0.7$ (Fig. 2), aligning with the maximum turnover rate dictated by the bone's specific surface area (Section 2.1.2).

2.1.2. Dependency on bone volume fraction: Specific surface and turnover rate

The turnover rate is determined by the specific surface area, defined as "internal surface area per unit volume of the bone" [14]. Mathematically, it is expressed as the void surface per total bone volume in the RVE ($S_\lambda = S_{\mathrm{Vd}}/V_{\mathrm{Tt.B}}$) [14] and can be expressed as a function of porosity:

$$
S_\lambda(f_{\mathrm{Tt.Po}}) = 32.2 f_{\mathrm{Tt.Po}} - 93.9 f_{\mathrm{Tt.Po}}^2 + 134 f_{\mathrm{Tt.Po}}^3 - 101 f_{\mathrm{Tt.Po}}^4 + 28.8 f_{\mathrm{Tt.Po}}^5. \tag{3}
$$

This polynomial relationship was fitted to experimental measurements of specific surface across a range of porosity values [14]. The polynomial relationship captures the dominant trend, with scatter (see also Fig. 6) reflecting the geometric variability in bone microstructure. Bones with equal porosity can have different specific surface values due to variations in pore sizes and shapes. Subsequent studies [37] validated and further refined this relationship. In dense bone, increasing porosity adds accessible surface, while in sparse trabecular bone, higher porosity reduces the remaining structural surface (Fig. 3).

Following Lerebours et al. [15], we assume turnover directly mirrors this geometric availability as formation and resorption depend on active bone cells that can only operate on available bone surfaces (Section 1). We calibrated the turnover rate to experimental data from Parfitt [38] (Fig. 3) via a scaling parameter c_{TR}

$$
\mathrm{TR}(f_{\mathrm{Tt.B}}) = c_{\mathrm{TR}} \cdot S_\lambda(f_{\mathrm{Tt.B}}), \tag{4}
$$

where $c_{\mathrm{TR}} = 5.961 \times 10^{-5}$ was determined by minimizing the sum of squared errors.

This feedback between porosity and turnover is fundamental to our model, as it dictates how remodeling-driven mineralization varies across the full porosity range. The turnover rate follows a non-monotonic trend, where decreasing bone volume fraction increases available surface area in dense cortical bone but reduces it in sparse trabecular networks (Fig. 3).

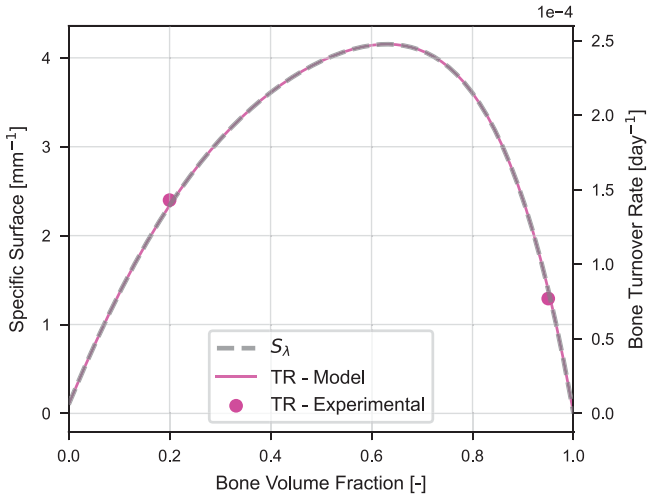


Fig. 3. Bone turnover rate and specific surface depending on bone volume fraction: The specific surface curve (S_λ, dashed line, left y-axis) represents the polynomial fit (Eq. (3)) to a point cloud from Martin [14]. The turnover rate (TR, solid line, right y-axis) was determined by scaling this specific surface relationship to match experimental bone turnover data (data points, right y-axis) from Parfitt [38].

2.1.3. Mineralization depending on aging tissue

After establishing porosity-dependent cell concentrations and turnover rates, we now address how these dynamics influence bone mineralization. We implement the first-in-first-out queuing algorithm developed by Martínez-Reina et al. [31] to track bone tissue age (defined as the time elapsed since formation).

The aging queue (Fig. 4) at time step t_i,

$$\mathscr{B}^{t_i} = \left[B_0^{t_i}, B_1^{t_i}, \dots, B_j^{t_i}, \dots, B_{n-1}^{t_i}, B_n^{t_i}\right], \tag{5}$$

consists of elements $B_j^{t_i}$, each representing bone tissue added at day t_{i-j} that is not yet fully resorbed. The double-indexing notation is necessary because the element does not simply represent all bone volume formed j days ago; rather, it accounts for the fraction that remains after daily resorption.

The queue is updated at each time step following a forward Euler algorithm. The step size (Δt) is the difference between current (t_i) and subsequent time step (t_{i+1}).

1. Newly formed bone volume enters at index zero:

$$\mathscr{B}^{t_{i+1}}[0] = B_0^{t_{i+1}} = f_{\mathrm{BF}}^{t_{i+1}}, \tag{6}$$

with formed bone volume fraction,

$$f_{\mathrm{BF}}^{t_{i+1}} = \Delta t \cdot \mathrm{BFR} \cdot C_{\mathrm{Ob_a}}(t_{i+1}, f_{\mathrm{Tt.B}}).$$

2. Existing elements advance one position (aging) and are partially resorbed. Following the mineralization lag time (Mlt), defined as mean time interval between the deposition of unmineralized bone matrix and the onset of its mineralization [35], elements are reduced proportionally to their size. The size of an element refers to the bone volume fraction stored in that queue element, and "proportional" means that resorption occurs according to the element's percentage of the total bone volume fraction at that time step. This results in

$$\mathscr{B}^{t_{i+1}}[j+1] = B_{j+1}^{t_{i+1}} = \begin{cases} B_j^{t_i}, & \text{if } j \le \mathrm{Mlt} \\ B_j^{t_i}\left(1 - \frac{f_{\mathrm{BRs}}^{t_i}}{f_{\mathrm{Tt.B}}^{t_i}}\right), & \text{if } j > \mathrm{Mlt} \end{cases} \tag{7}$$

with resorbed bone volume fraction,

$$f_{\mathrm{BRs}}^{t_i} = \Delta t \cdot \mathrm{BRs.R} \cdot C_{\mathrm{Oc_a}}(t_i, f_{\mathrm{Tt.B}}).$$

In steady-state, $f_{\mathrm{Tt.B}}^{t_i} = f_{\mathrm{Tt.B}}^{t_{i+1}}$, holds for all i. During initialization, the last element of the queue (index n) is used to ensure mass conservation by storing any remaining bone volume fraction:

$$\mathscr{B}^{t_{i+1}}[n] = B_n^{t_{i+1}} = f_{\mathrm{Tt.B}}^{t_{i+1}} - \sum_{i=0}^{n-1} B_i^{t_{i+1}}. \tag{8}$$

Once steady-state is reached, the entire bone volume fraction is distributed across elements with ages less than n, making the last element zero.

3. Let t_R be the time a bone patch remains in the queue until fully resorbed. Since our queue length n is designed to exceed t_R, the total bone volume fraction is distributed across the first t_R elements, with later elements remaining zero. Consequently, the total bone volume fraction must equal the sum of all queue elements:

$$\sum_{i=0}^{t_R} B_i^{t_{i+1}} = f_{\mathrm{Tt.B}}^{t_{i+1}}. \tag{9}$$

Unlike earlier models limited by queue capacity [31], our vectorized approach handles over 40,000 elements, ensuring the entire tissue lifespan is captured without residual elements.

This algorithm supports time-dependent and steady-state simulations. This study specifically analyzes bone remodeling under steady-state conditions. We initialize the queue with all-zero elements and iteratively update them until the initial bone volume fraction is distributed across queue elements and equilibrium is reached, characterized by constant queue values.

Each element accumulates mineral based on its age according to a refined exponential law [33,39] including lag phase of duration Mlt during which no mineralization occurs, followed by primary and secondary phase:

$$M(t) = \begin{cases} 0, & \text{if } t \le \mathrm{Mlt} \\ M_{\max}(1 - e^{-\mathrm{MAR}(t-\mathrm{Mlt})}), & \text{if } t > \mathrm{Mlt} \end{cases} \tag{10}$$

where MAR is the mineralization rate and $M_{\max}$ is the maximum mineral content. Parameter values are given in the Supplementary Material. The average mineral volume fraction is then calculated as the weighted sum of all queue elements:

$$f_M^{t_i} = \frac{\sum_{j=0}^{t_R} B_j^{t_i} \cdot M(j)}{f_{\mathrm{Tt.B}}^{t_i}}. \tag{11}$$

Both numerator and denominator represent volume fractions of the RVE, ensuring the result is mineral content per bone volume.

Bone material density (Dn.mat) is determined by the volume fractions of mineral, organic and water phases [31] following

$$\mathrm{Dn.mat} = \mathrm{Dn.M} \cdot f_M + \mathrm{Dn.O} \cdot f_O + \mathrm{Dn.W} \cdot f_W, \tag{12}$$

where f_O and f_W are the volume fractions of organic material and water relative to $V_{\mathrm{Tt.B}}$. The volume fraction of organic material is assumed to be constant [24,30,33] with water being progressively replaced by mineral [40]: $f_M + f_O + f_W = 1$. Apparent density is defined in [30] as

$$\mathrm{Dn.app} = \mathrm{Dn.mat} \cdot f_{\mathrm{Tt.B}}. \tag{13}$$

The average material and apparent density can be calculated depending on the average mineral content after initialization of the queue as $f_M = f_M^{t_R}$ (Eq. (11)). This framework enables a unified analysis of mineralization dynamics across the full porosity range under steady-state conditions.

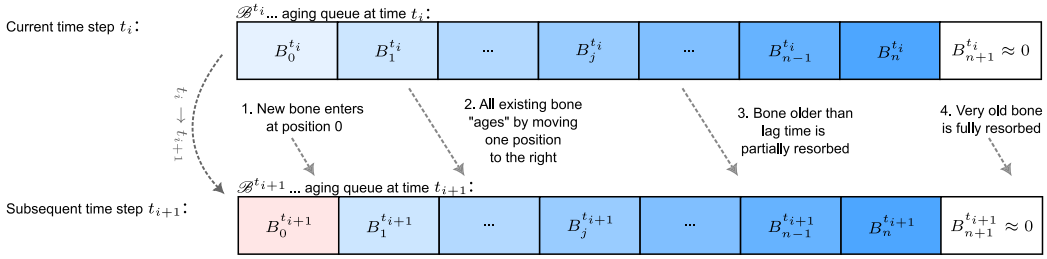


Fig. 4. Illustration of the aging queue: This graph shows how bone remodeling is tracked over time. The queue manages newly formed bone patches as they age, with elements being updated at each time step to account for formation, maturation, and eventual resorption. Element size determines how these processes are quantified in the model.

2.2. Parameter identification

Because measuring mineralization rates directly is experimentally challenging, we calibrate MAR by minimizing the least-squares error between simulated and experimental density data [23]. Following the modeling framework in Hypothesis 3 (Section 2.4), the objective function ($E = E(\mathrm{MAR})$) is defined as

$$E = \sum_{i=0}^{n} \left(\frac{\mathrm{Dn.app}^{\mathrm{exp}}(f^i_{\mathrm{Tt.B}}) - \mathrm{Dn.app}^{\mathrm{sim}}(f^i_{\mathrm{Tt.B}})}{\Delta \mathrm{Dn.app}^{\mathrm{exp}}} \right)^2 + \left(\frac{\mathrm{Dn.mat}^{\mathrm{exp}}(f^i_{\mathrm{Tt.B}}) - \mathrm{Dn.mat}^{\mathrm{sim}}(f^i_{\mathrm{Tt.B}})}{\Delta \mathrm{Dn.mat}^{\mathrm{exp}}} \right)^2, \tag{14}$$

where Δ denotes the experimental densities range, $f^i_{\mathrm{Tt.B}}$ represent specific bone volume fractions. The experimental material and apparent density are denoted by $\mathrm{Dn.mat}^{\mathrm{exp}}$ and $\mathrm{Dn.app}^{\mathrm{exp}}$. The corresponding simulated densities are denoted by $\mathrm{Dn.mat}^{\mathrm{sim}}$ and $\mathrm{Dn.app}^{\mathrm{sim}}$. We minimize Eq. (14) using a bounded minimization algorithm (L-BFGS-B), with parameter bounds informed by Martínez-Reina et al. [31].

2.3. Sensitivity analysis

We conduct a sensitivity analysis using Sobol' indices [41] to determine the impact of three key parameters – mineralization lag time (Mlt), mineral apposition rate (MAR), and maximum mineral content (M_{max}) – on characteristic boomerang-shaped relationship. These parameters directly control the mineralization process (Eq. (10)), while other model parameters are either biologically constrained or have negligible impact on the steady-state of bone remodeling. We define a proximity metric, P, to quantify the density divergence between the cortical and trabecular extremes:

$$P(\mathrm{params}) = \mathrm{Dn.mat}(0.9, \mathrm{params}) - \mathrm{Dn.mat}(0.1, \mathrm{params}), \tag{15}$$

with $\mathrm{params} = \{\mathrm{Mlt}, \mathrm{MAR}, M_{\mathrm{max}}\}$. A small value of P indicates similar densities, resulting in a boomerang profile. A large value of P indicates divergent densities, leading to a more monotonic relationship. We choose this proximity measure as a computationally efficient approach, despite the availability of more complex shape comparison metrics. Parameter ranges were determined based on [30]: $M_{\mathrm{max}} \in [0.1, 1]$, $\mathrm{Mlt} \in [0, 100]$ days, $\mathrm{MAR} \in [10^{-5}, 10^{-2}]$. First- and second-order indices were calculated using Saltelli's sampling scheme ($N = 2^{10}$) via the SALib library [42,43] to account for both individual (first-order) and interactive (second-order) effects on the variance of P.

2.4. Formulation of hypotheses

We analyze biological mechanisms that might drive the observed relationship between apparent and material density. We propose three hypotheses, following previous work [16].

Hypothesis 1. The turnover rate differences explain the mineral content variations with porosity.

This base case represents the model framework described in Section 2.1. It assumes that variations in mineral content are driven solely by turnover rates governed by specific surface area. We maintain consistency across the porosity range for all other biological and mineralization parameters.

Hypothesis 2. Combined effects of porosity-dependent turnover rate and targeted resorption in different bone compartments determine the mineral content variations with porosity.

This hypothesis posits that osteoclasts preferentially target older bone tissue with higher mineral content while maintaining the first hypothesis. Less mineralized regions are indicative of recently formed bone, which may be temporarily protected from resorption. Targeted resorption does not violate the steady-state assumption of the system: while individual bone packets are selectively resorbed based on age or mineral content, the overall balance between formation and resorption rates remains equal.

We implement this concept through two approaches. First, we restrict the second update rule (Eq. (7)) of the queuing algorithm to

$$\mathscr{B}^{t_{i+1}}[j+1] = B^{t_{i+1}}_{j+1} = \begin{cases} B^{t_i}_j, & \text{if } j < t_{\mathrm{pref}} \\ B^{t_i}_j \left(1 - \frac{f^{t_i}_{\mathrm{BRs}}}{f^{t_i}_{\mathrm{Tt.B}}}\right), & \text{if } j \geq t_{\mathrm{pref}} \end{cases} \tag{16}$$

with targeted resorption of bone patches older than a preferential age t_{pref}.

The second approach follows Berli et al. [24], who studied the boomerang-shaped curve relating apparent and material density using basic multicellular units (BMUs). BMUs are temporary, spatially organized groups of osteoclasts and osteoblasts responsible for bone remodeling. Their work assumes that BMUs in trabecular bone resorb half the area (semi-osteon) compared to those in cortical bone (osteon). We implement this by scaling the resorption rate as

$$\overline{\mathrm{BRs.R}}(f_{\mathrm{Tt.B}}) = \begin{cases} \mathrm{BRs.R}/2, & \text{if } f_{\mathrm{Tt.B}} \leq 0.3 \\ \mathrm{BRs.R} \cdot (f_{\mathrm{Tt.B}} + 0.2), & \text{if } 0.3 < f_{\mathrm{Tt.B}} < 0.8 \\ \mathrm{BRs.R}, & \text{otherwise.} \end{cases} \tag{17}$$

Hypothesis 3. Both turnover rate and mineralization kinetics differences explain the mineral content variations with porosity.

We propose that mineralization kinetics vary with porosity, while maintaining the first hypothesis. This is supported by possible differences in ion accessibility and mineral accumulation rate, as discussed in the introduction. We replace the constant mineral apposition rate in Eq. (10) with a porosity-dependent function:

$$\mathrm{MAR}(f_{\mathrm{Tt.B}}) = \frac{\mathrm{MAR}_{\mathrm{ref}}}{f_{\mathrm{Tt.B}}}, \tag{18}$$

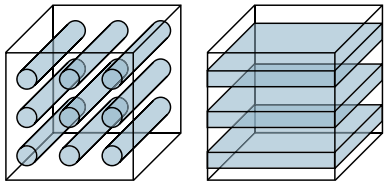


Fig. 5. Idealized trabecular geometries: A cubic volume of interest (Le^3) containing either rod- or plate-dominated structures. While a parallel arrangement is shown for clarity, the derived specific surface relationships depend only on scalar geometric parameters, not on specific structural organization.

where MAR_{ref} is the reference rate from Hypothesis 1. This formulation captures the inverse relationship between mineralization rate and bone volume fraction.

2.5. Modeling morphological variation and dispersion

The experimental apparent-vs-material density relationship shows significant dispersion in the mid-range of bone volume fractions. Trabecular bone consists of a mix of rods and plates, and the relative proportions of these structures can differ even when bone volume fractions are the same. We hypothesize that this scatter arises from morphological variability — specifically the heterogeneous mix of rods and plates in trabecular bone [44]. While two regions may exhibit an identical bone volume fraction ($f_{\mathrm{Tt.B}}$), their specific surface area can vary depending on their micro-architectural organization. We suggest that the extreme cases of exclusively rod-like or plate-like structures define the bounds of the experimental data cloud. To quantify this, we analyzed the specific surface (S_λ) of two idealized geometries within a volume of interest of length Le. (Fig. 5).

We recall the definition of specific surface: $S_\lambda = \frac{S_V}{V_{\mathrm{Tt.RVE}}}$. For rod-dominated structures (number N.Ro, radius Rd), it holds that

$$f^{\mathrm{Ro}}_{\mathrm{Tt.B}} = \frac{V^{\mathrm{Ro}}_{\mathrm{Tt.B}}}{V_{\mathrm{Tt.RVE}}} = \frac{\mathrm{N.Ro}\cdot\pi\cdot\mathrm{Rd}^2}{\mathrm{Le}^2},\ S^{\mathrm{Ro}}_\lambda = \frac{S^{\mathrm{Ro}}_V}{V_{\mathrm{Tt.RVE}}} = \frac{\mathrm{N.Ro}\cdot 2\pi\cdot\mathrm{Rd}}{\mathrm{Le}^2}. \quad (19)$$

For plate-dominated structures (number N.Pl, thickness Th), it holds that

$$f^{\mathrm{Pl}}_{\mathrm{Tt.B}} = \frac{V^{\mathrm{Pl}}_{\mathrm{Tt.B}}}{V_{\mathrm{Tt.RVE}}} = \frac{\mathrm{N.Pl}\cdot\mathrm{Th}}{\mathrm{Le}},\ S^{\mathrm{Pl}}_\lambda = \frac{S^{\mathrm{Pl}}_V}{V_{\mathrm{Tt.RVE}}} = \frac{\mathrm{N.Pl}\cdot 2}{\mathrm{Le}}. \quad (20)$$

Comparing the specific surface relationships $S^{\mathrm{Ro}}_\lambda / S^{\mathrm{Pl}}_\lambda$ for a given value $f_{\mathrm{Tt.B}}$ such that $f_{\mathrm{Tt.B}} = f^{\mathrm{Ro}}_{\mathrm{Tt.B}} = f^{\mathrm{Pl}}_{\mathrm{Tt.B}}$, it follows that

$$\mathrm{N.Pl} = \frac{\mathrm{N.Ro}\cdot\pi\cdot\mathrm{Rd}^2}{\mathrm{Th}\cdot\mathrm{Le}}, \quad (21)$$

and ultimately

$$\frac{S^{\mathrm{Ro}}_\lambda}{S^{\mathrm{Pl}}_\lambda} = \frac{\mathrm{Th}}{\mathrm{Rd}}. \quad (22)$$

Martin's original work on specific surface theory [14] proposed boundary curves to encapsulate most measured data points of specific surface with notable dispersion in the mid-range of bone volume fractions (Fig. 6). We generate analogous boundaries by applying multiplication factors to the specific surface equation (Eq. (3)) in our model.

For rod-dominated structures at a fixed bone volume fraction, the specific surface is inversely proportional to the rod radius

$$S^{\mathrm{Ro}}_\lambda = \frac{2\cdot f^{\mathrm{Ro}}_{\mathrm{Tt.B}}}{\mathrm{Rd}}. \quad (23)$$

For a given porosity, smaller rod radii result in higher specific surface area and consequently higher turnover rates, affecting mineral content distribution. This shows how structural factors control bone remodeling dynamics beyond bone volume fraction.

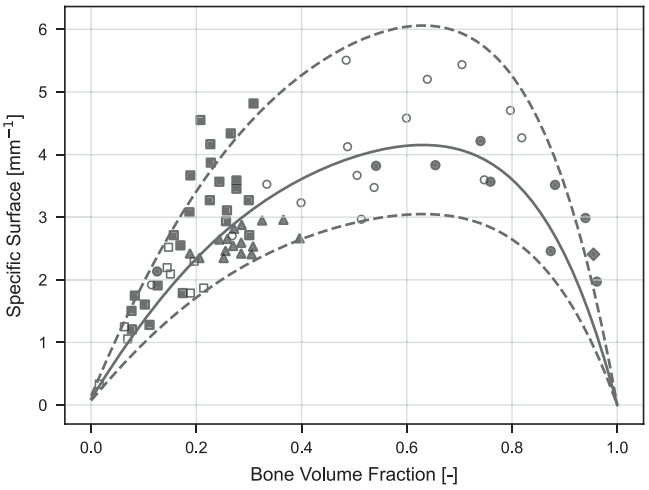


Fig. 6. Specific surface with experimental data: The S_λ-curve (Eq. (3), solid) is scaled (dashed) by 1.459 (top) and 0.734 (bottom) to enclose the majority of data points. Symbols denote healthy (solid) and diseased (open) human bone from multiple anatomical sites circles: femoral bone (circles); iliac crest (squares); rib (diamonds); vertebra (triangles). The figure was adapted from Martin [14] and Pivonka et al. [36], which contain original data and details.

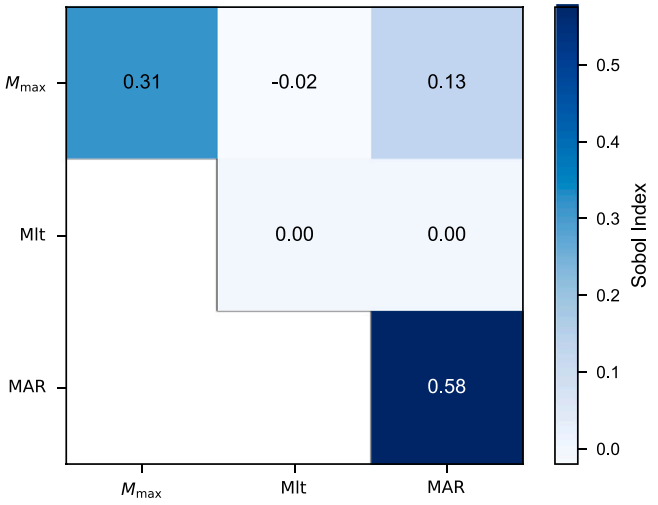


Fig. 7. Sobol' sensitivity analysis: mineral apposition rate (MAR) and its interaction with maximum mineral content (M_{max}) dominate model variance, mineralization lag time (Mlt) has no significant contribution. First-order indices explain variance by individual parameters, while second-order indices show variance explained by parameter interactions. Negligible negative values represent numerical noise.

3. Results

3.1. Parameter sensitivity

The mineral apposition rate is the most important factor in controlling mineralization patterns in our model, as shown in our sensitivity analysis (Fig. 7). The model is most sensitive to variations in mineral apposition rate (highest first order index), particularly when interacting with maximum mineral content (highest second order index). Total-order indices assign MAR a contribution of 62.4% to the total model output variance, followed by M_{max} with 37.6% and Mlt with 0.1%. This highlights the importance of porosity-dependent mineralization kinetics in analyzing experimental observations (Hypothesis 3).

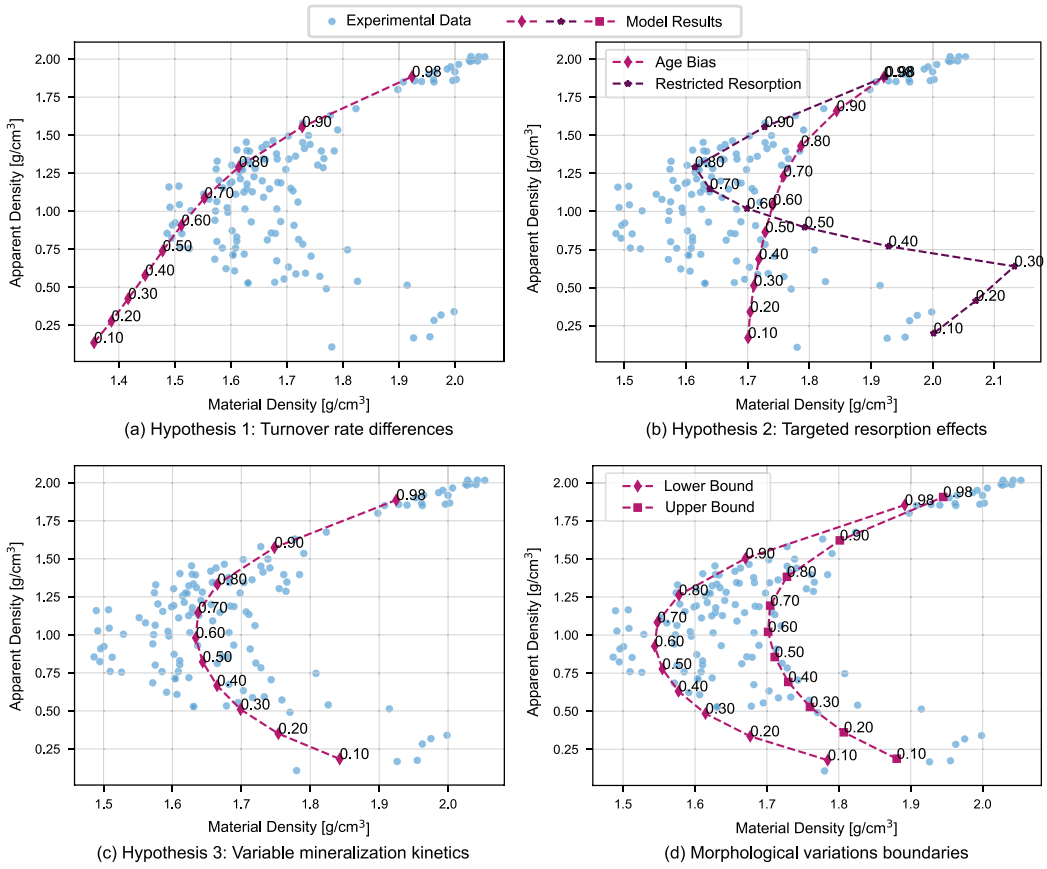


Fig. 8. Comparison of mineralization hypotheses and microarchitectural effects on density relationships. Labels next to data points show bone volume fractions. (a) Hypothesis 1 fails to capture the boomerang shape using only turnover variations. (b) Hypothesis 2 (targeted resorption) partially replicates the trend but fails in the low bone volume fraction range. (c) Hypothesis 3 (porosity-dependent kinetics) fully reproduces the experimental boomerang curve. (d) The rod-to-plate morphological boundaries (Section 2.5) successfully enclose the experimental data cloud, explaining the observed dispersion.

3.2. Dependence of mineralization dynamics on porosity

For the first hypothesis relying on turnover differences alone (Hypothesis 1), our model produces values within the correct range for both apparent and material density and successfully replicates the cortical branch of the experimental data (Fig. 8a). However, it fails to reproduce the characteristic boomerang-shaped curve observed experimentally. The model correctly shows that apparent density increases with increasing material density for denser bone structures, but it does not capture the inverse relationship expected at lower bone volume fractions. Our findings do not support the hypothesis that turnover rate differences alone explain the variations in mineral densities between cortical and trabecular bone.

Targeted resorption by osteoclasts (Hypothesis 2) is modeled based on either preferential age (Eq. (16)) or modification of the resorption rate (Eq. (17)). Using the first approach, the model accurately reproduces the upper branch (cortical bone) and transition towards the central region of the data cloud, but fails to capture the return along the lower branch (trabecular bone) (Fig. 8b). Instead of bending back toward higher material density values, the simulated trajectory drops almost vertically beyond the turning point, missing the characteristic boomerang-like distribution observed in the experimental data. The second approach partially replicates the experimental data trend but deviates in regions of lower bone fractions ($\lesssim 0.3$) corresponding to trabecular bone (Fig. 8b). The model curve for mid-range and lower bone volume fractions appears offset from the center of the experimental data cloud, while the cortical branch aligns well with experimental measurements. The second approach implements two key methodological concepts: (1) determining cell concentration (particularly active osteoclasts) based on specific surface area, and (2) applying a bone volume fraction-dependent restriction to the resorption rate (Eq. (17)). We note that the effect of bone volume fraction is considered twice: in calculating the cell concentrations; and in modifying the resorption rate of active osteoclasts.

Our sensitivity analysis shows that mineral apposition kinetics are a primary driver of model variance. Hypothesis 3 assumes that both turnover and mineral apposition rate depend on porosity. This approach successfully reproduces the characteristic boomerang-shaped curve observed in experimental data as well as the value range, suggesting that porosity-dependent mineralization kinetics are essential for the relationship between bone structure and mineralization patterns (Fig. 8c).

3.3. Impact of morphological variation on density patterns

To account for the experimental data dispersion, we established a framework to model the influence of micro-architectural heterogeneity. We derived boundaries that largely enclose our experimental mineral density data (Fig. 8d) by applying multiplication factors to the specific surface equation (Eq. (3)). The upper bound represents the plate-dominated extreme, while the lower bound represents the rod-dominated extreme as derived above.

The ratio of boundary S_λ-curves ($1.459/0.734 \approx 1.99$) closely matches the theoretical rod-to-plate ratio (Th/Rd = 81 μm/44.15 μm

≈ 1.83) derived from human morphometric analysis [45]. Values were collected from trabecular bone samples from multiple donors to capture the natural variability in trabecular geometries [45]. This validates our geometric interpretation: dispersion is driven by rod-plate heterogeneity in the mid-range (0.3–0.8 $f_{Tt.B}$), while the more homogeneous configurations at extreme porosities reduce variance.

Detailed mineralization queue dynamics including distribution patterns are provided in Appendix A.

4. Discussion

This study introduces a mathematical framework that captures the relationship between material and apparent density across the full porosity range. Our sensitivity analysis (Section 3.1) identified the mineral apposition rate (MAR) as the primary contributor (62.4%) to model variance. This quantitative result justifies focusing on porosity-dependent mineralization kinetics as the likely mechanism behind the observed density patterns. By incorporating porosity-dependent turnover and mineral apposition rate, our approach replicates the boomerang-shaped curve observed in experimental studies without assuming osteoclastic targeted resorption. Although physiologically coherent, our results suggest that targeted resorption alone cannot explain this behavior.

Hypothesis 1 attributed this variation solely to differences in turnover rate based on the validated concept of specific surface [14,37]. We found that this mechanism alone could not reproduce the experimental curve for trabecular bone (Fig. 8a). Hypothesis 2 introduced targeted resorption through age-based restrictions on younger bone patches and porosity-dependent resorption rate based on Berli et al.'s model [24]. While Hypothesis 2 partially replicated the boomerang curve (Fig. 8b), it introduced a methodological inconsistency. By applying a resorption restriction based on bone volume fraction while already accounting for cell concentration via specific surface area, the model effectively 'double-counts' the influence of porosity. This suggests that a more consistent framework should rely on either surface availability or resorption restrictions, but not both simultaneously.

Hypothesis 3, which integrates porosity-dependent turnover and mineral apposition rate, aligns most closely with both experimental data and physiological reasoning (Fig. 8c). Trabecular bone is highly vascularized but lacks the dense intracortical vascular network present in cortical bone, and blood vessels are not in immediate proximity to the mineralizing bone surface [46]. Nutrient and ion supply therefore relies on diffusion, resulting in different local concentrations of calcium and phosphate ions and a distinct physicochemical environment. These differences likely influence the kinetics of hydroxyapatite precipitation [12]. Trabecular bone has a higher turnover rate due to its role in calcium homeostasis and its unique microarchitecture, which results in a higher surface-area-to-volume ratio [14,37]. Together, these factors support the porosity-dependent mineralization behavior caused by variations in turnover and mineral apposition rate. Our findings are consistent with the work of Lerebours et al. [16], who demonstrated higher mineral content in cortical compared to trabecular bone and hypothesized underlying differences in mineralization kinetics.

The dispersion observed in the mid-porosity range is well-explained by micro-architectural heterogeneity. Our geometric analysis (Section 2.5) confirms that the dispersion boundaries (Fig. 8d) correspond to the theoretical ratio of rod-to-plate geometries derived from literature [45]. While cortical bone shows tighter clustering due to the more uniform osteonal architecture [47], the wide dispersion in trabecular regions reflects the varying proportions of rods and plates in different anatomical sites.

Direct comparison of our results with human bone mineralization data is challenging, as no comparable dataset of mineral density across the full porosity range currently exists. Farlay et al. (2022) [48] analyzed 60 iliac biopsies from untreated postmenopausal osteoporotic women, examining mineralization at the bone structural unit (BSU) level. They distinguished between osteonal and interstitial bone within cortical and trabecular compartments. The study reported unexpectedly small differences in degree of mineralization of bone (DMB) (1.029 ± 0.043 g/cm^3 for cortical and 1.003 ± 0.031 g/cm^3 for trabecular bone) when considering whole compartments as well as at the BSU level (Table 1 in [48]). Differences between cortical and trabecular bone were substantially smaller than differences between osteonal and interstitial bone within each compartment. This suggests that microstructural organization may play a more significant role. The authors proposed that better accessibility of calcium and phosphate ions in trabecular bone could influence mineralization kinetics, or alternatively, that differential regulation mechanisms may prevent cortical bone from becoming overmineralized. Both explanations align with our hypothesis of porosity-dependent mineral apposition rates driven by distinct physicochemical microenvironments. Farlay et al. (2019) [49] analyzed transiliac biopsies from 20 healthy pre- and postmenopausal women and found cortical DMB of approximately 1.02 g/cm^3 and trabecular DMB of approximately 1.00 g/cm^3 (Fig. 1 in [49]), with trabecular bone volume fraction of 21.9 ± 6.2% (Table 1 in [49]). These small differences in material density despite substantial variations in porosity between compartments are consistent with our model results and the underlying data. Similar patterns were observed by Nuzzo et al. [50] in their analysis of iliac crest specimens from osteoporotic patients before and after treatment, with cortical and trabecular compartments showing DMB values in a comparable range and minimal differences between compartments (Table 1 in [50]). The DMB values reported in these iliac crest studies are lower than the material density range in our study (1.4–2.1 g/cm^3). Differences in anatomy and mechanical environment could cause this discrepancy, as the iliac crest experiences relatively lower mechanical demands and the elephant femur bears substantial weight-bearing loads. Zioupos et al. [51] also analyzed 67 human femoral heads from fracture patients and reported trabecular material density values that fall within the same range as their elephant bone measurements (Fig. 4 in [51]). Data points are similar to the lower branch of the boomerang-shaped material-apparent density relationship. This cross-species consistency in the fundamental relationship between material and apparent density, despite absolute value differences across anatomical sites, validates the generalizability of our porosity-dependent mineralization framework. The pattern that emerges across these independent datasets – similar material densities between cortical and trabecular bone at the tissue level, combined with the characteristic boomerang curve spanning the full porosity range – demonstrates that our model captures physiologically relevant mineralization behavior that transcends specific anatomical locations and species.

Our model focuses on tissue scale porosity as the primary determinant of mineralization differences between cortical and trabecular bone, without explicitly incorporating the lacunar-canalicular network (LCN). While the LCN is essential for nutrient exchange, the available evidence on how LCN properties systematically differ between cortical and trabecular bone is scarce, with reported variations confounded by differences in species, anatomical site, and developmental history [52,53]. We therefore assumed its contribution to be relatively uniform across bone compartments at the scale of our analysis. Recent high-resolution synchrotron micro-computed tomography (microCT) studies by Gauthier et al. [54,55] revealed differences in LCN architecture between osteonal and interstitial bone tissue. LCN properties have been shown to influence local mineral content [56–58]. However, these observations pertain to microstructural distinctions within cortical bone rather than systematic differences between cortical and trabecular compartments. It could be hypothesized that trabecular bone – characterized by higher turnover – might exhibit different LCN characteristics than cortical bone with more interstitial tissue, but direct comparative data remain scarce. Given the current evidence, we consider tissue scale porosity to be the dominant factor driving the compartmental differences we observe, consistent with the hypothesis

testing of Lerebours et al. (2020) [16] and supported by physiological reasoning regarding nutrient supply and physicochemical microenvironment [12]. As research on the LCN's influence on mineralization kinetics continues to advance, future refinements to our framework may need to incorporate LCN-related parameters.

We acknowledge several limitations. The experimental data used for validation originates from a single bone sample of an elephant [23]. The source publication provides justification for the applicability of the results in a human context. We substantiated the applicability by using human data to obtain the boundary curves in Section 2.5. Computationally, the aging queue implementation requires substantial memory and time resources, particularly for long-term simulations. While currently feasible in steady-state simulations, optimization strategies may be necessary for broader applications. Additionally, some model parameters – such as ligand–receptor binding rates – cannot be measured experimentally. However, these values have been established in prior validated BCPMs, reducing the impact of this limitation. The timescale for mineralization in our model follows an exponential law reaching a plateau over several years. While some experimental studies suggest shorter duration, our choice aligns with established numerical frameworks [31,39] that account for the long-term variability in mineral density distribution. Our model is built upon published and validated models and theories [14,15,30,31]; our results are consistent with the hypotheses testing from Lerebours et al. [16]; and our results show consistency with known physiology.

Future efforts will extend this framework to bone pathologies and mechanical feedback loops. By assigning local Young's moduli based on porosity-dependent ash fractions [10], this model provides a foundation for multiscale coupling with finite element analysis (FEA). While current results establish the compositional basis for investigating bone quality, a complete characterization of bone stiffness and strength may require accounting for the structural orientation of collagen [40,59,60]. Future work will address algorithmic optimization of the aging queue to support the computational demands of long-term, organ-scale modeling.

5. Conclusion

This study introduces a novel mathematical framework that explicitly models bone mineralization dynamics as a function of porosity. Our model successfully reproduces the characteristic boomerang-shaped relationship between material and apparent density across varying porosity. Systematic hypothesis testing shows that combined effects of porosity-dependent turnover rate and mineral apposition rate best explain this relationship. The demonstrated link between porosity and mineralization dynamics represents a step toward more comprehensive bone quality modeling.

CRediT authorship contribution statement

Corinna Modiz: Writing – original draft, Visualization, Software, Methodology, Formal analysis, Conceptualization. **Natalia M. Castoldi:** Writing – review & editing, Supervision, Conceptualization. **Jose L. Calvo-Gallego:** Writing – review & editing, Methodology. **Stefan Scheiner:** Writing – review & editing, Supervision. **Vittorio Sansalone:** Writing – review & editing, Supervision. **Saulo Martelli:** Writing – review & editing, Supervision. **Javier Martínez-Reina:** Writing – review & editing, Supervision, Methodology, Formal analysis. **Peter Pivonka:** Writing – review & editing, Supervision, Conceptualization.

Declaration of competing interest

The authors of this manuscript have nothing to declare.

Acknowledgments

We gratefully acknowledge funding received through the Australian Research Council, Australia [IC190100020; DP230101404]. Javier Martínez Reina and José Luis Calvo Gallego would like to acknowledge funding provided by the Ministerio de Ciencia, Innovación *y* Universidades/ Agencia Estatal de Investigación of the Spanish Government through the research project PID2024-161475OB-I00 entitled "Integración de un modelo de remodelación ósea *y* un modelo de homeostasis del Ca. Predicción de riesgo de fractura osteoporótica. Diseño de tratamientos de paciente-específico".

Appendix A. Mineralization dynamics in high versus low porosity

We can analyze the distribution of total bone volume fraction ($f_{\mathrm{Tt.B}}$) throughout the aging queue and the detailed mineralization patterns across different porosities. By mapping mineral content to each element in the aging queue, we create a "mineral queue" that visualizes mineralization within a specific RVE. While our model cannot reproduce conventional BMDD curves as it relies on averaged bone volume fractions without spatial information, it provides insight into mineralization at the RVE level with specific porosity.

The distribution pattern of bone volume fraction ($f_{\mathrm{Tt.B}}$) in the aging queue shows distinct characteristics. Elements within the mineralization lag time (unaffected by resorption) contain the highest bone volume fractions, decreasing over time due to ongoing resorption. In cortical bone, the bone volume fraction is distributed across more queue elements, with each element containing a higher fraction of bone volume (Fig. A.9a,blue).

Mineral content follows our porosity-dependent mineralization law (Hypothesis 3, Section 3.2), increasing more rapidly for lower bone volume fractions and approaching maximum mineral content exponentially (Fig. A.9b). The model combines aging queue distribution with mineralization law, leading to a specific relationship between element size and mineral content. Young elements contain little mineral due to low mineralization, while old elements contain little mineral due to their small volume despite being highly mineralized. Elements with intermediate bone volume fractions have the highest mineral content levels, leading to a right-skewed mineralization distribution (Fig. A.9c). Similar to classical BMDD curves, we observe a shift in the distribution peak when comparing different total bone volume fractions (e.g., 0.3 versus 0.8).

The relationship between element size and mineral content shows that (Fig. A.9d) newly formed, larger elements start with minimal mineral content (osteoid in mineralization lag time). As elements decrease in size due to resorption, their mineral content increases. However, there is an inflection point where, despite increasing mineral density, the total mineral content per element start to decrease as it is multiplied by the diminishing bone volume.

Appendix B. Supplementary data

Supplementary material related to this article can be found online at https://doi.org/10.1016/j.bone.2026.117905.

Data availability

The code used in this study is available in the GitHub repository [61]. The repository contains all relevant scripts, model implementations, and documentation necessary to reproduce the results presented in this work.

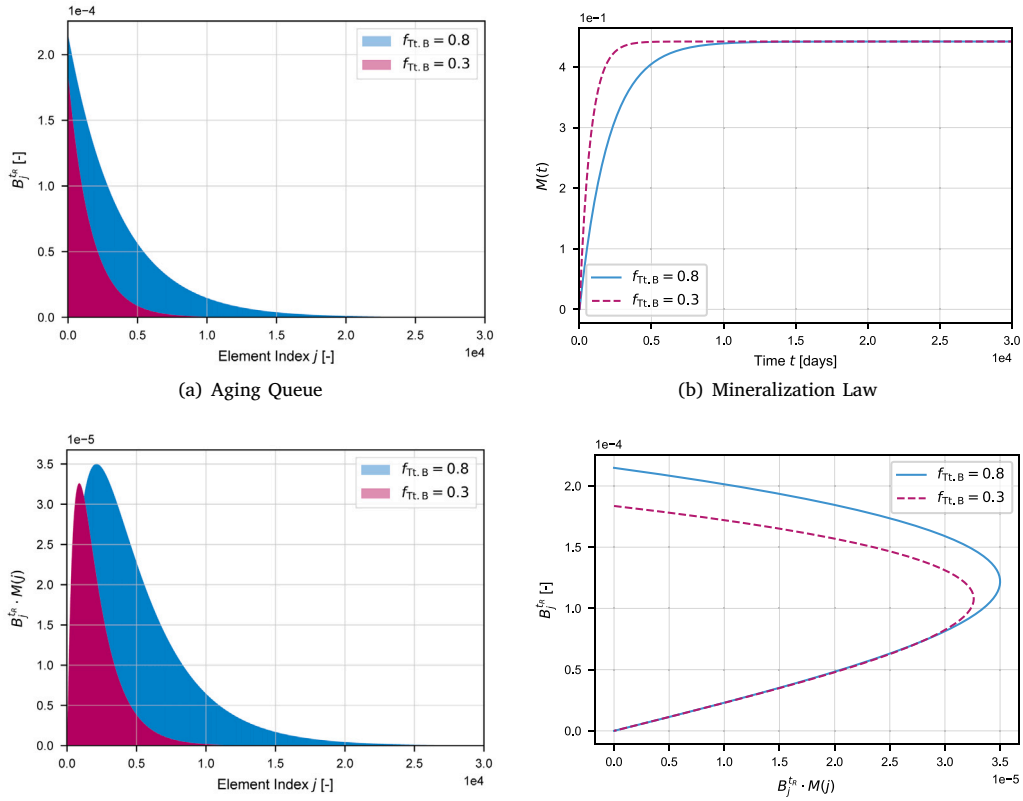


Fig. A.9. Mineralization and aging properties for two different bone volume fractions: (a) The aging queue distributes the total bone volume fraction across its elements according to formation and resorption activities. (b) The mineralization law determines the mineral content depending on the age of the bone patch. (c) Combining (a) and (b) determines the mineral content attached to the bone volume fraction in the aging queue elements. (d) The relationship between bone volume fraction and assigned mineral content of a queue element is initially inverse – as one decreases, the other increases – up to an inflection point, beyond which the relationship becomes direct, with both decreasing.

References

[1] R. Bartl, C. Bartl, Bone Disorders, first ed., Springer International Publishing, 2017, http://dx.doi.org/10.1007/978-3-319-29182-6.

[2] G. Boivin, P.J. Meunier, The mineralization of bone tissue: a forgotten dimension in osteoporosis research, Osteoporos Int. 14 (S3) (2003) 19–24, http://dx.doi.org/10.1007/s00198-002-1347-2.

[3] G. Boivin, P. Chavassieux, A. Santora, J. Yates, P. Meunier, Alendronate increases bone strength by increasing the mean degree of mineralization of bone tissue in osteoporotic women, Bone 27 (5) (2000) 687–694, http://dx.doi.org/10.1016/s8756-3282(00)00376-8.

[4] G. Boivin, P.J. Meunier, Effects of bisphosphonates on matrix mineralization, J. Musculoskelet. Neuron. Interact. 2 (6) (2002) 538–543.

[5] G. Boivin, P. Meunier, The degree of mineralization of bone tissue measured by computerized quantitative contact microradiography, Calcif. Tissue Int. 70 (6) (2002) 503–511, http://dx.doi.org/10.1007/s00223-001-2048-0.

[6] G. Boivin, Y. Bala, A. Doublier, D. Farlay, L. Ste-Marie, P. Meunier, P. Delmas, The role of mineralization and organic matrix in the microhardness of bone tissue from controls and osteoporotic patients, Bone 43 (3) (2008) 532–538, http://dx.doi.org/10.1016/j.bone.2008.05.024.

[7] G. Boivin D. Farlay, Bone mineral quality, InTech (2012) 3–32, http://dx.doi.org/10.5772/29091, Ch. 1.

[8] A.A. Al-Bari, A. Al Mamun, Current advances in regulation of bone homeostasis, FASEB BioAdvances 2 (2020) 668–679, http://dx.doi.org/10.1096/fba.2020-00058.

[9] M. Murshed, Mechanism of bone mineralization, Cold Spring Harb. Perspect. Med. 8 (12) (2018) 1–11, http://dx.doi.org/10.1101/cshperspect.a031229.

[10] C.J. Hernandez, T.S. Keller G.S. Beaupré, D.R. Carter, The influence of bone volume fraction and ash fraction on bone strength and modulus, Bone 29 (1) (2001) 74–78, http://dx.doi.org/10.1016/s8756-3282(01)00467-7.

[11] P. Roschger, B.M. Misof, K. Klaushofer, Basic aspects of bone mineralization, osteoporosis, in: Contemporary Endocrinology, Springer International Publishing, 2020, pp. 89–113, http://dx.doi.org/10.1007/978-3-319-69287-6_5.

[12] H. Poorhemati, S.V. Komarova, Mathematical model capturing physicochemical and biological regulation of bone mineralization, Sci. Rep. 14 (1) (2024) http://dx.doi.org/10.1038/s41598-024-81472-1.

[13] G. Osterhoff, E.F. Morgan, S.J. Shefelbine, L. Karim, L.M. McNamara, P. Augat, Bone mechanical properties and changes with osteoporosis, Injury 47 (2016) S11–S20, http://dx.doi.org/10.1016/S0020-1383(16)47003-8.

[14] B.R. Martin, Porosity and specific surface of bone, Crit. Rev. Biomed. Eng. 10 (3) (1984) 179–222.

[15] C. Lerebours, P. Buenzli, S. Scheiner, P. Pivonka, A multiscale mechanobiological model of bone remodelling predicts site-specific bone loss in the femur during osteoporosis and mechanical disuse, Biomech. Model. Mechanobiol. 15 (2015) http://dx.doi.org/10.1007/s10237-015-0705-x.

[16] C. Lerebours, R. Weinkamer, A. Roschger, P.R. Buenzli, Mineral density differences between femoral cortical bone and trabecular bone are not explained by turnover rate alone, Bone Rep. 13 (2020) http://dx.doi.org/10.1016/j.bonr.2020.100731.

[17] G. Boivin, P.J. Meunier, Changes in bone remodeling rate influence the degree of mineralization of bone, Connect. Tissue Res. 43 (2–3) (2002) 535–537, http://dx.doi.org/10.1080/03008200290000934.

[18] J.F. Griffith, K. Engelke, H.K. Genant, Looking beyond bone mineral density: Imaging assessment of bone quality, Ann. New York Academy Sci. 1192 (1) (2010) 45–56, http://dx.doi.org/10.1111/j.1749-6632.2009.05378.x.

[19] E. Donnelly, D.X. Chen, A.L. Boskey, S.P. Baker, M.C.H. van der Meulen, Contribution of mineral to bone structural behavior and tissue mechanical properties, Calcif. Tissue Int. 87 (5) (2010) 450–460, http://dx.doi.org/10.1007/s00223-010-9404-x.

[20] A. Bigi, G. Cojazzi, S. Panzavolta, A. Ripamonti, N. Roveri, M. Romanello, K. Noris Suarez, L. Moro, Chemical and structural characterization of the mineral phase from cortical and trabecular bone, J. Inorg. Biochem. 68 (1) (1997) 45–51, http://dx.doi.org/10.1016/S0162-0134(97)00007-X.

[21] K. Choi, S.A. Goldstein, A comparison of the fatigue behavior of human trabecular and cortical bone tissue, J. Biomech. 25 (12) (1992) 1371–1381, http://dx.doi.org/10.1016/0021-9290(92)90051-2.

[22] S. Nuzzo, F. Peyrin, P. Cloetens, J. Baruchel, G. Boivin, Quantification of the degree of mineralization of bone in three dimensions using synchrotron radiation microtomography, Med. Phys. 29 (11) (2002) 2672–2681, http://dx.doi.org/10.1118/1.1513161.
[23] P. Zioupos, R.B. Cook, J.R. Hutchinson, Some basic relationships between density values in cancellous and cortical bone, J. Biomech. 41 (9) (2008) 1961–1968, http://dx.doi.org/10.1016/j.jbiomech.2008.03.025.
[24] M. Berli, C. Borau, O. Decco, G. Adams, R.B. Cook, J.M. García Aznar, P. Zioupos, Localized tissue mineralization regulated by bone remodelling: A computational approach, PLoS One 12 (3) (2017) http://dx.doi.org/10.1371/journal.pone.0173228.
[25] V. Lemaire, F.L. Tobin, L.D. Greller, C.R. Cho, L.J. Suva, Modeling the interactions between osteoblast and osteoclast activities in bone remodeling, J. Theoret. Biol. 229 (3) (2004) 293–309, http://dx.doi.org/10.1016/j.jtbi.2004.03.023.
[26] P. Pivonka, J. Zimak, D.W. Smith, B.S. Gardiner, C.R. Dunstan, N.A. Sims, T. John Martin, G.R. Mundy, Model structure and control of bone remodeling: A theoretical study, Bone 43 (2) (2008) 249–263, http://dx.doi.org/10.1016/j.bone.2008.03.025.
[27] S. Scheiner, P. Pivonka, C. Hellmich, Coupling systems biology with multiscale mechanics, for computer simulations of bone remodeling, Comput. Methods Appl. Mech. Engrg. 254 (2013) 181–196, http://dx.doi.org/10.1016/j.cma.2012.10.015.
[28] J.L. Calvo-Gallego, P. Manchado-Morales, P. Pivonka, J. Martínez-Reina, Spatio-temporal simulations of bone remodelling using a bone cell population model based on cell availability, Front. Bioeng. Biotechnol. 11 (2023) http://dx.doi.org/10.3389/fbioe.2023.1060158.
[29] R. Ruiz-Lozano, J.L. Calvo-Gallego, P. Pivonka, M.M. McDonald, J. Martínez-Reina, An in silico approach to elucidate the pathways leading to primary osteoporosis: age-related vs. postmenopausal, Biomech. Model. Mechanobiol. 23 (4) (2024) 1393–1409, http://dx.doi.org/10.1007/s10237-024-01846-2.
[30] J. Martínez-Reina, P. Pivonka, Effects of long-term treatment of denosumab on bone mineral density: insights from an in-silico model of bone mineralization, Bone 125 (2019) 87–95, http://dx.doi.org/10.1016/j.bone.2019.04.022.
[31] J. Martínez-Reina, J. García-Aznar, M. Doblaré J. Domínguez, On the role of bone damage in calcium homeostasis, J. Theoret. Biol. 254 (3) (2008) 704–712, http://dx.doi.org/10.1016/j.jtbi.2008.06.007.
[32] M. Welsch T. Blöß, RVE procedure for estimating the elastic properties of inhomogeneous microstructures such as bone tissue, in: Biomedical Technology. Lecture Notes in Applied and Computational Mechanics, Vol. 74, Springer, Cham, 2015, pp. 1–17, http://dx.doi.org/10.1007/978-3-319-10981-7_1, Ch. 1.
[33] N.M. Castoldi, E. Pickering, V. Sansalone, D. Cooper, P. Pivonka, Bone turnover and mineralisation kinetics control trabecular bmdd and apparent bone density: insights from a discrete statistical bone remodelling model, Biomech. Model. Mechanobiol. 23 (3) (2024) 893–909, http://dx.doi.org/10.1007/s10237-023-01812-4.
[34] A. Zaoui, Continuum micromechanics: Survey, J. Eng. Mech. 128 (8) (2002) 808–816, http://dx.doi.org/10.1061/(ASCE)0733-9399(2002)128:8(808).
[35] D.W. Dempster, J.E. Compston, M.K. Drezner, F.H. Glorieux, J.A. Kanis, H. Malluche, P.J. Meunier, S.M. Ott, R.R. Recker, A.M. Parfitt, Standardized nomenclature, symbols, and units for bone histomorphometry: A 2012 update of the report of the asbmr histomorphometry nomenclature committee, J. Bone Miner. Res. 28 (1) (2012) 2–17, http://dx.doi.org/10.1002/jbmr.1805.
[36] P. Pivonka, P.R. Buenzli, S. Scheiner, C. Hellmich, C.R. Dunstan, The influence of bone surface availability in bone remodelling - a mathematical model including coupled geometrical and biomechanical regulations of bone cells, Eng. Struct. 47 (2013) 134–147, http://dx.doi.org/10.1016/j.engstruct.2012.09.006.
[37] C. Lerebours, C.D.L. Thomas, J.G. Clement, P.R. Buenzli, P. Pivonka, The relationship between porosity and specific surface in human cortical bone is subject specific, Bone 72 (2015) 109–117, http://dx.doi.org/10.1016/j.bone.2014.11.016.
[38] A.M. Parfitt, The Physiologic and Clinical Significance of Bone Histomorphometric Data, CRC Press, Boca Raton, FL, 1983, Ch. 9.
[39] D. Ruffoni, P. Fratzl, P. Roschger, K. Klaushofer, R. Weinkamer, The bone mineralization density distribution as a fingerprint of the mineralization process, Bone 40 (5) (2007) 1308–1319, http://dx.doi.org/10.1016/j.bone.2007.01.012.
[40] D.B. Burr, Chapter 1 - bone morphology and organization, in: M. R. Allen D. B. Burr (Ed.), Basic and Applied Bone Biology, second ed., Academic Press, 2019, pp. 3–26.
[41] I.M. Sobol´, Global sensitivity indices for nonlinear mathematical models and their monte carlo estimates, Math. Comput. Simulation 55 (1–3) (2001) 271–280, http://dx.doi.org/10.1016/S0378-4754(00)00270-6.
[42] J. Herman T. Iwanaga, Toward SALib 2.0: Advancing the accessibility and interpretability of global sensitivity analyses, Socio-Environmental Syst. Model. 4 (2022) 18155, http://dx.doi.org/10.18174/sesmo.18155.
[43] J. Herman, W. Usher, SALib: An open-source python library for sensitivity analysis, J. Open Source Softw. 2 (9) (2017) http://dx.doi.org/10.21105/joss.00097.
[44] W.S.S. Jee, Bone mechanics handbook, in: Integrated Bone Tissue Physiology: Anatomy and Physiology, second ed., CRC Press, 2001, pp. 1–34.
[45] M. Stauber, R. Müller, Volumetric spatial decomposition of trabecular bone into rods and plates - a new method for local bone morphometry, Bone 38 (4) (2006) 475–484, http://dx.doi.org/10.1016/j.bone.2005.09.019.
[46] M. Brookes, W.J. Revell, Blood Supply of Bone: Scientific Aspects, Springer-Verlag, London, 1998, http://dx.doi.org/10.1007/978-1-4471-1543-4.
[47] A.J. Burghardt, H.R. Buie, A. Laib, S. Majumdar, S.K. Boyd, Reproducibility of direct quantitative measures of cortical bone microarchitecture of the distal radius and tibia by HR-pQCT, Bone 47 (3) (2010) 519–528, http://dx.doi.org/10.1016/j.bone.2010.05.034.
[48] D. Farlay, G. Falgayrac, S. Rizzo C. Ponçon, B. Cortet, R. Chapurlat, G. Penel, I. Badoud, P. Ammann, G. Boivin, Material and nanomechanical properties of bone structural units of cortical and trabecular iliac bone tissues from untreated postmenopausal osteoporotic women, Bone Rep. 17 (2022) 101623, http://dx.doi.org/10.1016/j.bonr.2022.101623.
[49] D. Farlay, Y. Bala, S. Rizzo, S. Bare, J.M. Lappe, R. Recker, G. Boivin, Bone remodeling and bone matrix quality before and after menopause in healthy women, Bone 128 (2019) 115030, http://dx.doi.org/10.1016/j.bone.2019.08.003.
[50] S. Nuzzo, M.-H. Lafage-Proust, E. Martin-Badosa, G. Boivin, T. Thomas, C. Alexandre, F. Peyrin, Synchrotron radiation microtomography allows the analysis of three-dimensional microarchitecture and degree of mineralization of human iliac crest biopsy specimens: effects of etidronate treatment, J. Bone Miner. Res. 17 (2002) 1372–1382, http://dx.doi.org/10.1359/jbmr.2002.17.8.1372.
[51] P. Zioupos, R. Cook, R. Aspden, A. Coats, Bone quality issues and matrix properties in OP cancellous bone, in: S. Dendorfer J. Hammer (Ed.), Medicine Meets Engineering: Proceedings of the 2nd Conference on Applied Biomechanics, IOS Press, 2008, pp. 238–245.
[52] P. Schneider, M. Meier, R. Wepf, R. Müller, Towards quantitative 3D imaging of the osteocyte lacuno-canalicular network, Bone 47 (5) (2010) 848–858, http://dx.doi.org/10.1016/j.bone.2010.07.026.
[53] G. Marotti V. Canè, G. Volpi, et al., Size and density of osteocyte lacunae in different regions of long bones, Calcif. Tissue Int. 34 (1982) 558–563, http://dx.doi.org/10.1007/BF02411304.
[54] R. Gauthier, H. Follet, C. Olivier, D. Mitton, F. Peyrin, 3D analysis of the osteonal and interstitial tissue in human radii cortical bone, Bone 127 (2019) 526–536, http://dx.doi.org/10.1016/j.bone.2019.07.028.
[55] R. Gauthier, H. Follet, C. Olivier, T. Lemaire, D. Mitton, F. Peyrin, Human cortical bone intrinsic permeability distribution based on 3D canalicular morphology, Bone 194 (2025) 117441, http://dx.doi.org/10.1016/j.bone.2025.117441.
[56] A. Roschger, P. Roschger, W. Wagermaier, J. Chen, A.F. van Tol, F. Repp, S. Blouin, A. Berzlanovich, G.M. Gruber, K. Klaushofer, P. Fratzl, R. Weinkamer, The contribution of the pericanalicular matrix to mineral content in human osteonal bone, Bone 123 (2019) 76–85, http://dx.doi.org/10.1016/j.bone.2019.03.018.
[57] B. Hesse, P. Varga, M. Langer, A. Pacureanu, S. Schrof, H. Suhonen N. Männicke, P. Maurer, P. Cloetens, F. Peyrin, K. Raum, Canalicular network morphology is the major determinant of the spatial distribution of mass density in human bone tissue: evidence by means of synchrotron radiation phase-contrast nano-CT, J. Bone Miner. Res. 30 (2015) 346–356, http://dx.doi.org/10.1002/jbmr.2324.
[58] M. Kerschnitzki, P. Kollmannsberger, M. Burghammer, G.N. Duda, R. Weinkamer, W. Wagermaier, P. Fratzl, Architecture of the osteocyte network correlates with bone material quality, J. Bone Miner. Res. 28 (2013) 1837–1845, http://dx.doi.org/10.1002/jbmr.1927.
[59] M.-G. Ascenzi, A. Benvenuti, A. Ascenzi, Single osteon micromechanical testing, in: Mechanical Testing of Bone and the Bone-Implant Interface, CRC Press, 1999, pp. 271–290.
[60] M.-G. Ascenzi, J. Gill, A. Lomovtsev, Orientation of collagen at the osteocyte lacunae in human secondary osteons, J. Biomech. 41 (16) (2008) 3426–3435, http://dx.doi.org/10.1016/j.jbiomech.2008.09.010.
[61] C. Modiz, Bone models, in: Version 1.0, University of Technology, Queensland, 2025, http://dx.doi.org/10.25912/RDF_1742263438470, https://github.com/cmodiz/Bone-Models.